# MPS and ACS with an atomic magnetometer

Simone Colombo $^{a,*}$  · Victor Lebedev $^a$  · Zoran D. Grujić $^a$  · Vladimir Dolgovskiy $^a$  · Antoine Weis $^a$ 

- <sup>a</sup>Département de Physique, Université de Fribourg, Chemin du Musée 3, 1700 Fribourg, Switzerland
- \*Corresponding author, email: simone.colombo@unifr.ch

#### **Abstract**

We show that a single atomic magnetometer in a magnetically unshielded environment can be used to perform magnetic particle spectroscopy (MPS) and AC susceptometry (ACS) on liquid-suspended magnetic nanoparticles. We demonstrate methods allowing a simultaneous recording of M(H) and dM/dH(H) dependences of samples containing down to 1  $\mu$ g of iron. Our results pave the way towards an atomic magnetometer based MPI scanner.

## I. Introduction

The technique of Magnetic Particle Imaging (MPI), following its introduction in 2005 [1], has evolved along two major pathways, viz., frequency-space MPI [2] and X-space MPI [3], both approaches having their respective merits and drawbacks. MPI relies on exciting a magnetic nanoparticle (MNP) sample by a monochromatically oscillating (frequency  $f_{scan}$ ) drive field  $H_{\rm scan}(t)$ —referred to as 'scan' field in this paperand detecting the polychromatic time-dependent magnetic induction  $B_{\rm NP}(t) \propto M_{\rm NP}$  that arises as a consequence of the nonlinear  $M_{\rm NP}(H_{\rm scan})$  relation. Most MPI approaches developed so far share the common feature that the detected signal  $S_{NP}(t)$  is recorded by induction coil(s). Because of Faraday's induction law, one has  $S_{\rm NP} \propto d B_{\rm NP}(t)/dt \propto d M_{\rm NP}(t)/dt \propto n f_{\rm scan}$ , where n denotes the order of the detected overtones, so that signal/noise considerations call for large drive frequencies. A high-frequency drive favors high speed operation permitting fast volumetric scans of the sample [4].

Frequency-domain operation profits from S/N ratio enhancement by selective bandpass-filtering of the harmonics at known frequencies, but involves demanding calibration procedures. X-space MPI, on the other hand, allows a simpler interpretation of the recorded (filtered) time series, leading to a computationally less demanding image reconstruction based on the a priori known field free point (or line) position. Both methods suffer from a direct strong drive field contribution to the detected induction. From the point of view of applying MPI to biological systems, in particular to humans, unwanted neural stimulation and unwanted side effects from excessive SAR (specific absorption rate) become pronounced at elevated frequencies and/or drive coil power [5].

Here we report on the detection of the anharmonic magnetic response of MNPs by a high sensitivity opti-

cally pumped atomic magnetometer (OPM), and demonstrate that an OPM can be used for Magnetic Particle Spectroscopy (MPS) and AC susceptometry (ACS). MPS is often referred to as zero-dimensional MPI, and any high-sensitivity MPS method is thus a necessary prerequisite for developing an MPI system.

Laser-driven OPMs are compact and versatile instruments, mostly operating at room temperature, that can detect magnetic field changes in the femto- or even subfemto-Tesla range. Recent review of various OPM principles and their applications is given in Ref. [6]. In the past decade OPMs have been deployed for biomagnetism studies, such as magnetocardiography [7, 8] and magnetoencephalography [9]. The suitability of OPMs for studying the magnetorelaxation of blocked MNPs was demonstrated in recent years [10, 11, 12]. More recently we have shown (Ref. [13] in this volume) that OPMs can also be used for the quantitative measurement of the saturation magnetization,  $M_S$ , the iron content and particle size distributions of aqueous MNP suspensions. We believe that because of their high sensitivity and large bandwidth (DC up to hundreds of kHz), OPMs, when combined with a variant of X-space MPI, have the potential to yield a complementary, low-frequency MPI technique.

## II. Experimental apparatus

The main components of the apparatus (mounted in a walk-in size double-layer aluminium chamber) are sketched in Figure 1. The MNP sample is excited by a periodically oscillating scan field  $H_{\rm scan}(t)$  produced by a 700 mm long, 14 mm diameter solenoid, next to which an identical, but oppositely poled solenoid reduces residual field at the OPM location (  $\sim$ 7 cm above the two solenoids) to  $\sim$ 1 nT per mT of scan field (more details are given in [13]).

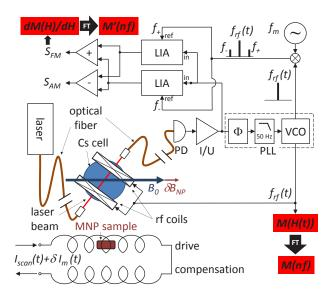


**Figure 1:** Sketch of the experimental setup. LIA: lock-in amplifier; PD: photodiode; I/U: transimpedance amplifier; VCO: voltage-controlled oscillator.  $f_{\pm}$  refers to frequencies  $f_{rf} \pm f_m$ .

The OPM is based on optically detected magnetic resonance in spin-polarized Cs vapor [7]. The sensor is operated in a homogeneous bias magnetic field  $B_0$  of 27  $\mu$ T, produced by large (~3×3×3 m³) Helmholtz coils, which also cancel the local laboratory field. We note that the MNP sample is also exposed to that bias field. The Cs spin polarization in the sensor precesses with a Larmor frequency  $f_{\mathrm{prec}}$  of 95 kHz in that field. The precession is driven phase-coherently by a weak (few nT) field oscillating at the 'rf' frequency  $f_{\rm rf}$  generated by a low bandwidth (~50 Hz) phase-locked loop (PLL, Fig. 1) ensuring that the magnetic resonance condition  $f_{\rm rf} = f_{\rm prec}$  is maintained when  $f_{\text{prec}}$ , i.e.,  $|\vec{B}_0|$  varies. The driven Cs spin precession impresses a modulation (at  $f_{rf}$ ) on the detected light power. The  $B_0$  field information is thus encoded in terms of the frequency  $f_{\rm rf} = \gamma_F |\vec{B}_0|$ , where  $\gamma_F \approx 3.5 \, {\rm Hz/nT}$ for Cs.

### III. Measurements and results

Small MNP-induced field changes  $|\delta \vec{B}_{NP}(t)| \ll |\vec{B}_0|$  in the total field at the sensor position  $\vec{B}_{tot}(t)$  yield corresponding OPM frequency changes

$$\delta f_{\rm NP}(t) = f(t) - f_0 = \gamma_F \left( |\vec{B}_{\rm tot}(t)| - |\vec{B}_0| \right)$$

$$= \gamma_F \delta \vec{B}_{\rm NP}(t) \cdot \hat{B}_0. \tag{1}$$

To first order in  $\delta B_{\rm NP}$  the OPM signal is thus determined by the projection  $\delta B_{\rm NP}(t) \equiv \vec{B}_{\rm NP}(t) \cdot \hat{B}_0$  of the field of interest onto the bias field, making the OPM an effective vector component magnetometer. The sensitivity to MNP signals will be maximized by having  $\vec{B}_0 \parallel \delta \vec{B}_{\rm NP}$ .

The HF2LI lock-in amplifier delivers a voltage  $S_{\delta f}(t) = \alpha \delta f_{\rm NP}(t)$ , which allows retrieving the corresponding detected induction change (Fig. 1).

#### III.I. Magnetization curve M(H)

Similarly to the method described in [13] we excite the sample by a field  $H_{\rm scan}(t)$  of amplitude  $\sim$  15 mT $_{pp}/\mu_0$  that sinusoidally oscillates at a frequency  $f_{\rm scan}$  of 600 mHz. We record time series (sampled at a rate of 320 S/s) of  $I_{\rm scan}(t)$  and the induced signals  $\delta B_{\rm NP}(t) = S_{\delta f}(t)/(\alpha \gamma_F)$ . These time-space results are shown as the lower two traces of Fig. 2. The recording was done on a 500  $\mu$ l EMG-707 sample containing 3.4 mg of iron (more details on the sample given in [13]).

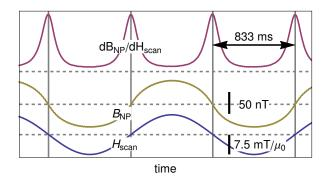


**Figure 2:** From bottom to top: Time series of the scan field  $H_{\rm scan}(t)$ , the corresponding induced  $\delta B_{\rm NP}(t) \propto M_{\rm NP}(t)$ , and  ${\rm d} B_{\rm NP}/{\rm d} H_{\rm scan}(t) \propto {\rm d} M_{\rm NP}/{\rm d} H_{\rm scan}(t)$  dependencies. The scan frequency was 600 mHz and the data shown are unfiltered raw data containing 533 data points per period.

Performing the Fourier transform of data from 30 consecutive scan cycles yields the harmonics spectrum

$$\widetilde{B}_{\rm NP}(f/f_{\rm scan}) = \mathscr{F}\left[\delta B_{\rm NP}(t)\right] = \mathscr{F}\left[\frac{S_{\delta f}(t)}{\alpha \gamma_F}\right]$$
 (2)

that can be rescaled to magnetization units by

$$M_{\rm NP} = \frac{4\pi R^3}{\mu_0 V_{\rm s}} \, \widetilde{B}_{\rm NP} \,, \tag{3}$$

where  $V_s$  is the sample volume and R the sample-magnetometer spacing (7 cm). The top graph of Fig. 3 shows such a Fourier spectrum. When rescaled to unity bandwidth, the noise floor in the figure represent a power spectral density of  $\sim 4 \text{ pT}/\sqrt{\text{Hz}}$  which limits the detectable number of harmonics in the M(H) signals to  $\approx 23$  for 3.4 mg of iron. The noise pedestal underlying the low-frequency Fourier components reflects low-frequency noise and drifts of the magnetic field at the sensor location. We draw attention to the fact that, conversely to conventional MPS methods, our technique gives also access to the fundamental frequency of the MNPs' magnetic response. In relation to the latter statement we also note that here we derive the harmonics

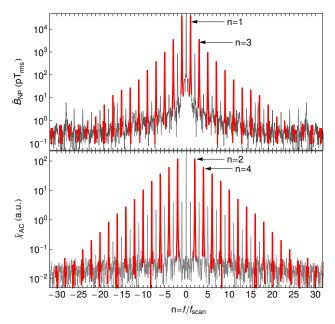


**Figure 3:** Fourier transforms of 30 cycles ( $\sim$ 50 s recording time) of  $B_{\rm NP}(t)$  and  ${\rm d}M/{\rm d}H(t)$  data as shown in Fig. 2. Top: Magnetic particle spectrum (MPS). Bottom: Fourier spectrum of AC susceptibility.

spectrum of  $\widetilde{M}_{NP}(f/f_{\text{scan}})$  from a direct measurement of  $M_{NP}(H(t))$ , while conventional MPS (and MPI) devices do the opposite, i.e., reconstruct  $M_{NP}(H)$  from recorded  $\widetilde{M}_{NP}(f/f_{\text{scan}})$  values.

## III.II. AC susceptibility $\chi_{AC} = dM/dH$

We have extended the method discussed above for measuring M(H) curves towards the direct and simultaneous recording of the derivative, i.e.,  $\mathrm{d}M/\mathrm{d}H(H)$ -dependence. For this we excite the sample with a bichromatic superposition of fields

$$H_{\text{scan}}^{\text{bi}}(t) = H_{\text{scan}}\cos(2\pi f_{\text{scan}}t) + \delta H_{\text{m}}\cos(2\pi f_{\text{m}}t), \quad (4)$$

with a scan field of amplitude  $H_{\rm scan} \sim 15~{\rm mT}_{pp}/\mu_0$  and a weaker modulation field  $\delta H_{\rm m} < 2~{\rm mT}_{pp}/\mu_0$ . The quasistatic scan at frequency  $f_{\rm scan} = 1~{\rm Hz} \ll f_{\rm m} = 753~{\rm Hz}$  implies that at any given time  $t_0$ , the MNPs' magnetization is given by  $M_{\rm NP}(t_0) = \sum_{n=0} m_n(t_0) \cos(n~2\pi f_{\rm m} t)$ , where  $m_0 \equiv M_{NP}[H_{\rm scan}(t_0)]$ , and where

$$m_{n>0}(t_0) = 4 \int_{f_{\rm m}t_0}^{f_{\rm m}t_0+\frac{1}{2}} M_{NP} \left[ H_{\rm scan}^{\rm bi}(t) \right] \cos(n2\pi f_{\rm m}t) d(f_{\rm m}t)$$

$$= \frac{2\delta H_{\rm m}}{n\pi} \int_{-1}^{1} M'_{NP} \left[ H_{\rm scan}^{\rm bi}(t_0;x) \right] \sqrt{1-x^2} U_{n-1}(x) dx. \quad (5)$$

In the last expression  $U_j$  is the j-th Chebyshev polynomial of the second kind. For  $\delta H_{\rm m} < H_k$ ,  $H_k$  being the samilar of the second kind. For  $\delta H_{\rm m} < H_k$ ,  $H_k$  being the samilar of the second kind. For  $\delta H_{\rm m} < H_k$ ,  $H_k$  being the samilar of the second kind. For  $\delta H_{\rm m} < H_k$ ,  $H_k$  being the samilar of the second kind. For  $\delta H_{\rm m} < H_k$ ,  $H_k$  being the samilar of the second kind. For  $\delta H_{\rm m} < H_k$ ,  $H_k$  being the samilar of the second kind.

ple's saturation field, the harmonic amplitudes  $m_{n>1}$  are negligible, and the first harmonic reduces to

$$m_1(t_0) = \delta H_{\rm m} \frac{d M_{\rm NP} [H_{\rm scan}(t_0)]}{d H} \equiv \delta H_{\rm m} M'_{NP} [H_{\rm scan}(t_0)] .$$
 (6)

At each time  $t_0$ , the magnetization component oscillating at  $f_m$  is thus proportional to the derivative of the MNPs' M(H) dependence (Langevin function).

We extract a signal proportional to  $m_1(H_{\rm scan}(t_0))$  in the following way: The sample's magnetization component  $m_0$  (varying at the slow frequency  $f_{\rm scan}$ ) and the sample's magnetization component  $m_1$  (oscillating at  $f_{\rm m}$ ) produce magnetic induction fields  $B_{\rm NP}(t_0)$  and  $\delta\,B_{\rm NP}(t_0)\cos(2\pi f_{\rm m}t)$ , respectively, that add to the offset field  $B_0$  at the sensor location.

The magnetometer signal is a photocurrent oscillating at a frequency proportional to the modulus of the total induction field

$$B_{\text{tot}}(t) = B_0 + B_{\text{NP}}(t_0) + \delta B_{\text{NP}} \cos(2\pi f_{\text{m}} t),$$
 (7)

where  $|B_{\rm NP}| \ll |B_0|$ . One sees that the problem of inferring the amplitude of the  $m_1(t)$  component is a problem of FM spectroscopy. The corresponding time-dependent photodiode signal is given by

$$U_{\rm PD}(t) = A(t)\cos\left[2\pi f_{\rm rf} t + \frac{f_{\rm p}}{f_{\rm m}}\sin\left(2\pi f_{\rm m}t\right)\right], \quad (8)$$

where  $f_p = \gamma_F \delta H_{\rm m}$ . Since the PLL is tracking slow variations  $B_{\rm NP}$  of  $B_0$  field, we have omitted, in Eq. 8, the contribution  $\gamma_F B_{\rm NP}(f_{\rm scan} t_0)$  to  $f_{\rm rf} = \gamma_F B_0$ . We extract the sideband amplitudes by the sideband demodulation technique illustrated in Fig. 1, which thus gives simultaneous access to both dM/dH(H) and M(H).

The top trace of Fig. 2 shows the derivative signal  $dB_{\rm NP}/dH_{\rm scan}(t)$ , which—after calibration by Eq. 3—is equivalent to  $dM_{\rm NP}/dH$ . The Fourier spectrum of 30 cycles of  $dB_{\rm NP}/dH_{\rm scan}(t)$  data is shown as lower graph in Fig. 3. Comparison of the two Fourier spectra reveals the superior power of FM-spectroscopy: While the direct M(H) method is sensitive to drift and low frequency noise of the 'background' field  $B_0$  at the sensor (as evidenced by the noise pedestal under the upper spectrum in Fig. 3), the derivative spectrum is insensitive to low-frequency changes of the carrier frequency  $f_{\rm rf}$ .

While the  $\widetilde{B}_{\rm NP}(f)$  spectrum is dominated by odd Fourier components, even frequency components dominate the

$$\widetilde{\chi}_{AC}(f) \propto \mathscr{F}\left[\frac{\mathrm{d}B_{\mathrm{NP}}(t)}{\mathrm{d}H}\right]$$
 (9)

spectrum.

The Fourier spectra show some artifacts. The upper graph of Fig. 3 contains a series of even harmonics arising from field components  $\delta \vec{B}_{\perp}(t)$  perpendicular to  $\vec{B}_0$ . Since  $|\vec{B}_{tot}(t)| = \sqrt{(B_0 + \delta B_{NP}(t))^2 + \delta B_1^2(t)}$  the signal

contains terms oscillating at even harmonics, the dominant one being at  $2f_{\rm scan}$ . In the lower graph of Fig. 3 the odd harmonics are mainly due to the fact that  $H_{\rm scan}$  does not oscillate around zero, but rather around the average value  $\langle H_{\rm scan} \rangle = B_0/\mu_0$  of 27  $\mu$ T/ $\mu_0$  (bias field).

In a series of dilution experiments we have demonstrated the proportional scaling of the M(H) [13] and  $\mathrm{d}M/\mathrm{d}H$  signals with iron content. Based on the lower graph of Fig. 3 that was recorded with 3.4 mg of iron, we estimate that our current detection limit in a recording time of 50 s is  $\sim$ 700 ng of iron.

#### IV. Conclusions and outlook

We have demonstrated that an atomic magnetometer in an unshielded environment can be used for a direct quantitative measurement of MPS and ACS spectra of magnetic nanoparticles in the sub-kHz frequency range. At current stage the method allows absolute iron content determinations at a sub- $\mu$ g level. The low-frequency scans give access to the response of large particles that are hydrodynamically blocked at the often used 25 kHz modulation frequency.

Because of the relatively slow ( $\approx$ 1 Hz) scan speed, the M(H)-recording is perturbed by magnetic field instabilities in our unshielded environment and suffers from low-frequency noise of the deployed scan current supply. As demonstrated in Ref. [7], a first- or second-order OPM gradiometer arrangement is able to improve the magnetometric sensitivity by up to two orders of magnitude. Work towards this goal is in progress.

We have also demonstrated a superior method that allows AC susceptometry  $(\mathrm{d}M/\mathrm{d}H)$  recordings based on an FM operation mode of the magnetometer. The latter approach gives direct access to the first harmonic response of the MNPs, information that is missing in standard MPI methods.

We note that the derivative curve  $\mathrm{d}M/\mathrm{d}H$ , when multiplied by a linear gradient field  $\mathrm{d}H/\mathrm{d}x$ , yields the point-spread function  $\mathrm{d}M/\mathrm{d}x$ , which—together with signal/noise considerations—defines the spatial resolution for X-space MPI [3]. Based on the excellent signal quality demonstrated above we now pursue the goal of designing a 2D X-space MPI scanner based on induction field detection by atomic magnetometers. In contrast to conventional pick-up coils that do not 'feel' inhomogeneous DC fields, the atomic sensor performance rapidly degrades in gradient fields, so that the main challenge will be the design of a gradient field generator that will be compatible with a high sensitivity mode of operation of the magnetometer.

**Acknowledgements.** This work was supported by Grant No. 200021\_149542 from the Swiss National Science Foundation.

#### References

- B. Gleich and J. Weizenecker. Tomographic imaging using the nonlinear response of magnetic particles. *Nature*, 435:1214–1217, 2005. doi: 10.1038/nature03808.
- [2] N. Panagiotopoulos, R. L. Duschka, M. Ahlborg, G. Bringout, Ch. Debbeler, M. Graeser, Ch. Kaethner, K. Lüdtke-Buzug, H. Medimagh, J. Stelzner, et al. Magnetic particle imaging: current developments and future directions. *International journal of nanomedicine*, 10:3097, 2015. doi: 10.2147/IJN.S70488.
- [3] P. W. Goodwill, E. U. Saritas, L. R. Croft, T. N. Kim, K. M. Krishnan, D. V. Schaffer, and S. M. Conolly. X-Space MPI: Magnetic Nanoparticles for Safe Medical Imaging. *Adv. Mater.*, 24:3870–3877, 2012. doi: 10.1002/adma.201200221.
- [4] J. Weizenecker, B. Gleich, and J. Borgert. Magnetic particle imaging using a field free line. J. Phys. D: Appl. Phys., 65:105009, 2008. doi: 10.1088/0022-3727/41/10/105009.
- [5] I. Schmale, B. Gleich, J. Rahmer, C. Bontus, J. Schmidt, and J. Borgert. MPI Safety in the View of MRI Safety Standards. *IEEE Trans. Magn.*, 51:6502604, 2015.
- [6] D. Budker and D.F. Jackson Kimball. Optical Magnetometry. Cambridge University Press, 2013.
- [7] G. Bison, N. Castagna, A. Hofer, P. Knowles, J. L. Schenker, M. Kasprzak, H. Saudan, and A. Weis. A room temperature 19channel magnetic field mapping device for cardiac signals. *Appl. Phys. Lett.*, 95(17), 2009.
- [8] O. Alem, T.H. Sanders, R. Mhaskar, J. Le Blanc, H. Eswaran, U. Steinhoff, Y. Okada, J. Kitching, L. Trahms, and S. Knappe. Fetal magnetocardiography measurements with an array of microfabricated optically pumped magnetometers. *Phys. Med. Biol.*, 60: 4797–4811, 2015. doi: 10.1088/0031-9155/60/12/4797.
- [9] T. H. Sander, J. Preusser, R. Mhaskar, J. Kitching, L. Trahms, and S. Knappe. Magnetoencephalography with a chip-scale atomic magnetometer. *Biomed. Opt. Expr.*, 3(5):981–990, 2012.
- [10] D. Maser, S. Pandey, H. Ring, M.P. Ledbetter, S. Knappe, J. Kitching, and D. Budker. Note: Detection of a single cobalt microparticle with a microfabricated atomic magnetometer. *Rev. Sci. Instrum.*, 82:086112, 2011. doi: 10.1063/1.3626505.
- [11] C. Johnson, N. L. Adolphi, K. L. Butler, D. M. Lovato, R. Larson, P. D. D. Schwindt, and E. R. Flynn. Magnetic relaxometry with an atomic magnetometer and SQUID sensors on targeted cancer cells. *J. Magn. Magn. Mater.*, 324(17):2613–2619, 2012. doi: 10.1016/j.jmmm.2012.03.015.
- [12] V. Dolgovskiy, V. Lebedev, S. Colombo, A. Weis, B. Michen, L. Ackermann-Hirschi, and A. Petri-Fink. A quantitative study of particle size effects in the magnetorelaxometry of magnetic nanoparticles using atomic magnetometry. J. Magn. Magn. Mater., 379:137–150, 2015. doi: 10.1016/j.jmmm.2014.12.007.
- [13] Simone Colombo, Victor Lebedev, Zoran Grujic, Vladimir Dolgovskiy, and Antoine Weis. M(h) dependence and size distribution of spions measured by atomic magnetometry. *Interna*tional Journal on Magnetic Particle Imaging, 2(1), 2016. ISSN 2365-9033. URL https://journal.iwmpi.org/index.php/ iwmpi/article/view/28.